Article

Optical properties of bcc transition metals in the range 0–40eV

ROMANIELLO, P., *et al*.

ROMANIELLO, P., *et al*. Optical properties of bcc transition metals in the range 0–40eV. *Physical review. B, Condensed matter and materials physics*, 2006, vol. 73, no. 7, p. 075115

DOI : 10.1103/PhysRevB.73.075115

Optical properties of bcc transition metals in the range 0–40 eV

P. Romaniello and P. L. de Boeij*
Theoretical Chemistry, Materials Science Centre, Rijksuniversiteit Groningen, Nijenborgh 4, 9747 AG Groningen, The Netherlands

F. Carbone and D. van der Marel
Département de Physique de la Matière Condensée, Universitée de Genève, CH-1211 Genève 4, Switzerland
(Received 27 September 2005; revised manuscript received 28 December 2005; published 23 February 2006)

We present a systematic analysis of the optical properties of bcc transition metals in the groups VB: V, Nb, and Ta, and VIB: paramagnetic Cr, Mo, and W. For this we use our formulation of time-dependent current-density-functional theory for the linear response of metals. The calculated dielectric and electron energy-loss functions are compared with our ellipsometry measurements and with data reported in literature, showing an overall good agreement. The experimental data of the dielectric functions presented by Nestell and Christy and by Weaver *et al.* differ mostly in the low-frequency region. However, we found that their reflectivity data are in very good agreement up to about 3 eV. We attribute this apparent discrepancy to the Drude-like extrapolation model used by Weaver *et al.* in the Kramers-Kronig procedure to extract the optical constants from their reflectivity data. Our experiments are in good agreement with Nestell and Christy's data. The calculated absorption spectra show some deviations from the experiments, in particular in the 3*d* metals. We assign the spectra in terms of transitions between pairs of bands and we analyze which parts of the Brillouin zone are mainly involved in the absorption. Our results suggest that the blueshift of some spectral features in our calculations can be attributed mainly to the incorrect description of the virtual *d* bands by the approximations used for the ground state exchange-correlation functional. These virtual bands are too weakly bound by the local density and generalized gradient approximations, in particular in the 3*d* metals. We calculate separately the inter- and intraband contributions to the absorption and we show using a $\mathbf{k}\cdot\mathbf{p}$ analysis that, within the scalar-relativistic approximation, interband transitions contribute to the absorption already at frequencies well below 0.5 eV. This finding makes questionable the Drude-like behavior normally assumed in the experimental analysis of the linear response. We find that the combination of the Drude model in which we use the calculated plasma frequency and an optimized relaxation time, and the calculated interband response can well describe the experimental spectra. The electron energy-loss spectra are very well reproduced by our calculations showing in each metal a dominant plasmon peak at about 22–24 eV, well above the corresponding Drude-like free-electron plasma frequency, and additional features in the range 10–15 eV. We show that the renormalization of the plasma frequency is due to the interplay between inter- and intraband processes, and that the additional features arise from the rich structure in the dielectric function caused by interband transitions.

DOI: 10.1103/PhysRevB.73.075115 PACS number(s): 71.45.Gm, 78.20.Ci

I. INTRODUCTION

The electronic structure of transition metals is in general characterized by the overlap and hybridization of nearly free-electron-like *sp* bands with a relatively narrower *d*-band complex. This leads to a rather complex Fermi surface with in general multiple sheets. Moving across a period the binding energy of the *d* bands drops with respect to the low-lying *sp* bands while at the same time the Fermi level rises within the *d* bands due to the increasing filling fraction. The width of the *d* bands first increases, reaching a maximum for the Cr group where the *d* bands are approximately half filled, and then decreases again. At the noble metals the *d* bands are completely filled and very narrow. Furthermore, progressing within the same group the width of the *d* bands increases. These trends in the band structure have a large influence on the optical properties of the transition metals. Optical experiments[1–6] have shown that the high-energy optical properties ($\hbar\omega \gtrsim 10$ eV) are very similar from metal to metal, but that the low-energy behavior varies significantly with the filling of the *d* bands. Transitions within these bands are responsible for the absorption in this spectral region. We have recently developed a method to treat the linear response of metal crystals within time-dependent current-density-functional theory (TDCDFT).[7] This method gave good results for the dielectric function and the electron energy-loss function of copper and silver already within the adiabatic local density approximation (ALDA). Furthermore, by treating the dominant scalar-relativistic effects (using the zeroth-order regular approximation) we obtained reasonable agreement with experiment also for the dielectric function of gold.[8] In the case of these noble metals, two main deviations of the calculated dielectric functions from experiments were pointed out: an increasing redshift of the whole absorption spectrum passing from Cu via Ag to Au, and the absence of the low-frequency Drude-like absorption. We speculated that the redshift is mainly due to the deficiency of the local density approximation in describing the correct position of the *d*-band complex with respect to the Fermi level in our ground-state calculation. The other deviation, instead, is in part a failure of the adiabatic approximation to the exchange-correlation functional used in the response calculation. The low-frequency Drude-like absorption is due to relaxation

processes such as electron-electron and electron-phonon scattering. The electron-electron scattering cannot be described within the ALDA in which a frequency-independent exchange-correlation kernel is used. More advanced frequency-dependent functionals will be needed to describe these relaxation effects. The inclusion of electron-phonon scattering requires a theory that goes beyond the pure electron density-functional description.[9] In this paper we use our method to investigate the optical properties of the bcc metals from group VB: V, Nb, and Ta, and from the adjacent group VIB: Cr (in the paramagnetic phase), Mo, and W. Unlike the noble metals, where the *d* bands are completely filled, these metals have partially filled *d* bands, thus the analysis of their absorption spectra in terms of direct transitions between *d* bands can give an insight into the performance of the LDA in describing the dispersion and the width of the *d* bands in 3*d*, 4*d*, and 5*d* metals, and of the ALDA in describing the response properties. Furthermore, these metals show interband absorption already at low frequencies, thus the separation in intra- and interband contributions to the absorption becomes difficult in the experimental analysis, where one often assumes the Drude-like behavior to hold at low frequency and well below the range of experimental data. Using the adiabatic local density approximation together with the long-wavelengh limit within our approach, we can calculate separately the inter- and intraband contributions to the dielectric function of these metals. We show that in these metals the interband absorption remains present at all frequencies, approaching a constant value for frequencies below $\simeq 0.5$ eV, unless spin-orbit effects are taken into account. In the latter case a small absorption gap appears. These findings make the straightforward use of the bare Drude model for the low-frequency range questionable. In order to compare our calculations with reliable experimental data we performed also spectroscopic ellipsometry in the energy range between 0.7 and 4.5 eV. The spectra have been acquired at room temperature and ambient pressure. All samples were polished before the measurements and kept in a nitrogen atmosphere during the spectra acquisition, in order to prevent oxidization. The experimental procedure is described in more detail in Sec. II. The rest of the paper is organized as follows. The theory underlying the dielectric and electron energy-loss function calculations, and the treatment of the scalar-relativistic effects within the zeroth-order regular approximation are briefly outlined in Sec. III. Details of the computational method can be found in Sec. IV. The optical properties of the group-VB transition metals V, Nb, and Ta, and of the group-VIB transition metals Cr, Mo, and W are discussed in Sec. V. Here by comparing our theoretical results with our recent ellipsometry measurements and with other experiments found in literature we give an insight into the trend of the optical properties of these metals with respect to the filling of the *d* bands. Finally in Sec. VI we draw conclusions about the performance of our method and of the exchange-correlation approximations used.

II. EXPERIMENTAL METHOD

The optical constants of the transition metals studied in this paper have been published in literature already several decades ago.[1–6,10,11] As these metals all have a bcc unit cell their optical constants are expected to be isotropic. Nestell, Johnson, and Christy[10,11] measured polycrystalline thin films evaporated *in situ*, and performed reflection and transmission experiments at normal and 60° angle of incidence to extract the optical constants *n* and *k* as a function of photon energy. Although this approach guarantees a negligible contribution from surface contamination, in particular from transition-metal oxides, still their optical constants showed a small but significant thickness dependence. Weaver and co-workers[1–6] measured the normal incidence reflectivity of polished single crystals and extracted the dielectric function via a standard Kramers-Kronig procedure. The dielectric functions presented by Weaver *et al.* deviate from Nestell and Christy's results mostly on the low-frequency side. However, the reflectivity data that we obtained from Nestell and Christy's results agree well with those by Weaver *et al.* at least up to 3 eV. This apparent discrepancy may be due to the Drude-like extrapolation model used in the Kramers-Kronig procedure needed to extract the optical constants from the reflectivity data. In this paper we question the validity of this Drude-like extrapolation for low frequency. The various sets of experiments show discrepancies in the absolute values of the optical constants, most notably for vanadium and chromium. Here we present our experimental results in the energy range between 0.7 and 4.5 eV obtained at room temperature using spectroscopic ellipsometry at an angle of incidence of 70° with a resolution of approximately 12 meV. The polycrystalline samples used had a purity of 99.99% and were polished with a diamond sand paper of 0.1-μm grain size until a mirrorlike surface was obtained. During the polishing process and the measurement the samples were kept in a pure nitrogen flow in order to prevent the oxidization of the surface. Our measurements are in excellent agreement with the results from Nestell and Christy for V and Cr where the various sets of experimental data differ most. For the other metals we find results in between the very similar data reported by Nestell and Christy and Weaver *et al.* Some departures at high frequencies between our experiments and those reported by Nestell, Johnson, and Christy may be due to the non-negligible surface roughness and the film morphology. Our ellipsometry experiments and the combination of reflection and transmission measurements by Nestell and Christy directly provide the real and the imaginary parts of the dielectric function without assuming any model *a priori*. Due to the large spectral range of Nestell and Christy's measurements and to their good agreement with our results we will consider them to be the reference data.

III. THEORY

We have recently extended the formulation of the time-dependent current-density-functional theory describing the linear response of nonmetallic crystals to macroscopic fields[12,13] to treat metals as well.[7] In this case not only transitions between occupied and unoccupied bands (interband contributions) contribute to the linear response, but also transitions within the same partially occupied band (intraband contributions) need to be considered. Within the adiabatic

TABLE I. Model parameters for the group-VB and -VIB metals. The plasma frequencies have been calculated directly from intraband response functions in the ALDA approximation. The relaxation times have been fitted to experiments in the frequency range 0–1 eV (see text). In our calculations we used the experimental lattice parameters listed here.

	V	Nb	Ta	Cr	Mo	W
a (Å)	3.02	3.30	3.31	2.88	3.15	3.16
ω_p (eV)	8.06	9.24	8.88	6.99	8.66	7.81
τ ($\times 10^{-15}$ s)	5.0±0.2[a]	4.09±0.12[a]	6.2±0.2[a]	3.78±0.03[a]	5.57±0.10	12.2±0.6[a]

[a]Standard deviation.

local density approximation (ALDA) and in the long-wavelength limit $q \to 0$ the two contributions remain separable, and we can calculate the dielectric function using the following expression:[7]

$$\epsilon(\omega) = [1 + 4\pi\chi_e^{inter}(\omega)] - \frac{4\pi i}{\omega}\sigma^{intra}(\omega). \quad (1)$$

Here the contribution in brackets is referred to as the interband part of the dielectric function and the last term on the right-hand side as the intraband contribution. The tensor components of the interband contribution to the electric susceptibility $\chi_e^{inter}(\omega)$ can be obtained by repeating an SCF response calculation of the interband contribution to the induced current density for the uniform macroscopic electric field in the three possible Cartesian directions $\hat{\mathbf{e}}$,

$$\chi_e^{inter}(\omega)\cdot\hat{\mathbf{e}} = \left(\frac{-i}{\omega V}\int \delta\mathbf{j}^{inter}(\mathbf{r},\omega)d\mathbf{r}\right)\Bigg|_{\mathbf{E}_{mac}=\hat{\mathbf{e}}}. \quad (2)$$

Analogously, the components of the intraband contribution to the macroscopic conductivity tensor $\sigma^{intra}(\omega)$ can be obtained from the intraband part via

$$\sigma^{intra}(\omega)\cdot\hat{\mathbf{e}} = \left(\frac{1}{V}\int \delta\mathbf{j}^{intra}(\mathbf{r},\omega)d\mathbf{r}\right)\Bigg|_{\mathbf{E}_{mac}=\hat{\mathbf{e}}}. \quad (3)$$

Once having calculated the macroscopic dielectric function $\epsilon(\omega)$, we can obtain also the electron energy-loss spectra by calculating the dynamical structure factor $S(\mathbf{q},\omega)$. This factor expresses the scattering rates in transmission energy-loss spectroscopy where one studies the inelastic scattering of a beam of high-energy electrons by a target. This structure factor is related to the imaginary part of the true density-density response function via the fluctuation-dissipation theorem,

$$S(\mathbf{q},\omega) = -2\,\mathrm{Im}\int\int e^{-i\mathbf{q}\cdot(\mathbf{r}-\mathbf{r}')}\chi(\mathbf{r},\mathbf{r}',\omega)d\mathbf{r}d\mathbf{r}'. \quad (4)$$

We retrieve in our approach the well-known result[14] that in the limit of vanishing q the dynamical structure factor is directly related to the macroscopic dielectric function according to the following relation:

$$\lim_{q\to 0}\frac{2\pi}{q^2V}S(\mathbf{q},\omega) = \mathrm{Im}\left\{\frac{-1}{\hat{\mathbf{q}}\cdot\epsilon(\omega)\cdot\hat{\mathbf{q}}}\right\}. \quad (5)$$

We have also included relativistic effects in our formulation[8] along the same line as Kootstra and co-workers.[15,16] They followed the description of van Lenthe and co-workers[17,18] and Philipsen *et al.*[19] by using the zeroth-order regular approximation (ZORA). Scalar-relativistic effects are then considered by using the ground-state scalar ZORA equation,

$$\left[-\nabla\cdot\frac{c^2}{2c^2 - v_{eff}(\mathbf{r})}\nabla + v_{eff}(\mathbf{r})\right]\psi_{i\mathbf{k}}(\mathbf{r}) = \epsilon_{i\mathbf{k}}\psi_{i\mathbf{k}}(\mathbf{r}), \quad (6)$$

to get the orbitals and the orbital energies needed in the response calculation, and by using the relativistic velocity operator,

$$\hat{\mathbf{v}} = -i[\mathbf{r},\mathcal{H}_{ZORA}] = -i\frac{c^2}{2c^2 - v_{eff}(\mathbf{r})}\nabla + \mathrm{H.a.}, \quad (7)$$

to calculate the induced current density, and hence the response functions of Eqs. (2) and (3). Here c is the velocity of light, $v_{eff}(\mathbf{r})$ is the self-consistent effective potential, and H.a. is the Hermitian adjoint expression. Spin-orbit effects have been studied only in the ground-state calculations by using the full ZORA Hamiltonian.

IV. COMPUTATIONAL METHOD

We calculated the optical dielectric functions $\epsilon(\omega)$ in the spectral range 0–10 eV for the isotropic crystals of vanadium, niobium, tantalum, paramagnetic chromium, molybdenum, and tungsten in a bcc lattice. We used the experimental lattice constants as listed in Table I. All calculations were performed using a modified version of the ADF-BAND program.[7,12,13,20–22] We checked that our results were converged with respect to the basis set size and the sampling density of the irreducible Brillouin zone. We made use of a hybrid valence basis set consisting of Slater-type orbitals (STOs) in combination with the numerical solutions of a free-atom Herman-Skillman program.[23] Cores were kept frozen up to $2p$ for V and Cr, $3d$ for Nb and Mo, and $4f$ for Ta and W. The spatial resolution of this basis is equivalent to a STO triple-zeta basis set augmented with two polarization functions.[24] The Herman-Skillman program also provides us

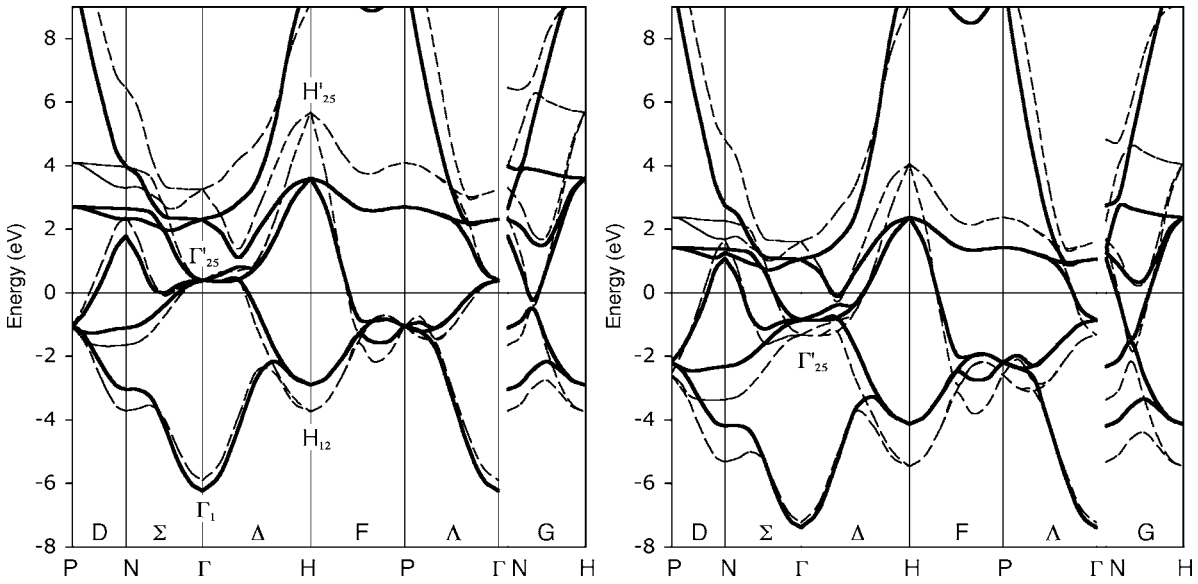

FIG. 1. Theoretical LDA ground-state band structures. The left panel shows vanadium (solid bold line) and niobium (dashed thin line), whereas the right panel shows chromium (solid bold line) and molybdenum (dashed thin line). The band structures reported for Nb and Mo refer to scalar-relativistic calculations.

with the free-atom effective potential. The crystal potential was evaluated using an auxiliary basis set of STO functions to fit the deformation density in the ground-state calculation and the induced density in the response calculation. For the evaluation of the k-space integrals in the ground-state calculations we used a quadratic numerical integration scheme, which was constructed by adopting a Lehmann-Taut tetrahedron method.[25,26] We found converged results using 84 sample points in the irreducible wedge of the Brillouin zone. In the response calculations the singular energy-dependent denominator in the response integrals is included in the quadrature weights of a linear tetrahedron method by using an analytic evaluation of the Cauchy principle value and residual parts. As we will show shortly below, in the scalar-relativistic calculations these metals exhibit interband absorption already in the spectral range $0-0.5$ eV, which involves transitions between bands degenerate at the Fermi level. A dense sampling of the Brillouin zone is then required in order to accurately describe the dispersions close to the Fermi surface. Therefore we used 1771 sample points for the response calculation in the low-frequency spectral region. Nevertheless, the results obtained for the lowest frequencies will still not be reliable due to the linear interpolation used in solving the k-space integrals. Therefore we made use of the $\mathbf{k}\cdot\mathbf{p}$ method of analytic continuation[27] near the points of degeneracy at the Fermi level to analyze the low-frequency interband transitions and the corresponding low-frequency behavior of the absorption. In all our ground-state calculations we used the local density approximation (LDA) for the exchange-correlation functional. In general the use of generalized-gradient approximations (GGAs) to the exchange-correlation functional is found to improve the ground-state properties of the $3d$ series,[28,29] whereas there have been mixed reports of their performance on the $4d$ and $5d$ series.[30–32] For comparison we have performed the calculation of the dielectric functions also by starting from ground states obtained at the GGA level, using the exchange-correlation functional proposed by Perdew and Wang (PW91),[33] and the one by Becke for the exchange[34] and Perdew for the correlation[35] (BP). The results, however, are very similar to those obtained at the LDA level. All results shown here were obtained using the Vosko-Wilk-Nusair parametrization[36] of the LDA exchange-correlation potential, which was also used to derive the ALDA exchange-correlation kernel for the response calculations.

V. RESULTS AND DISCUSSION

A. Band structure and Fermi surface

In Figs. 1 and 2 the calculated ground-state energy bands of V, Nb, and Ta (in the left panels), and Cr, Mo, and W (in the right panels) have been displayed along high-symmetry directions. The energy levels are reported with respect to the respective Fermi levels, in order to facilitate the comparison between the band structures. The valence bands are numbered at a given k point starting from the lowest band. Across the same group the band structures are quite similar, except that the d bands are broader, as immediately becomes clear by inspection of the d-band widths $E(H'_{25})-E(H_{12})$ in Figs. 1 and 2. Moving from the $3d$ series to the $5d$ series, the s-like Γ_1 state becomes more tightly bound, as result of a stronger stabilization by relativistic effects. The most noticeable difference between the band structures of the two groups is the position of the d-like Γ'_{25} states, which lie above the Fermi level for the group-VB metals but below this level for the group-VIB metals. The group-VB transition metals contain five valence electrons per atom, whereas the group-VIB ones contain six valence electrons. In the group-VB metals the lowest valence band and in the group-VIB metals the lowest two bands are completely filled. The second and third, respectively, the third, fourth, and fifth bands, are partially

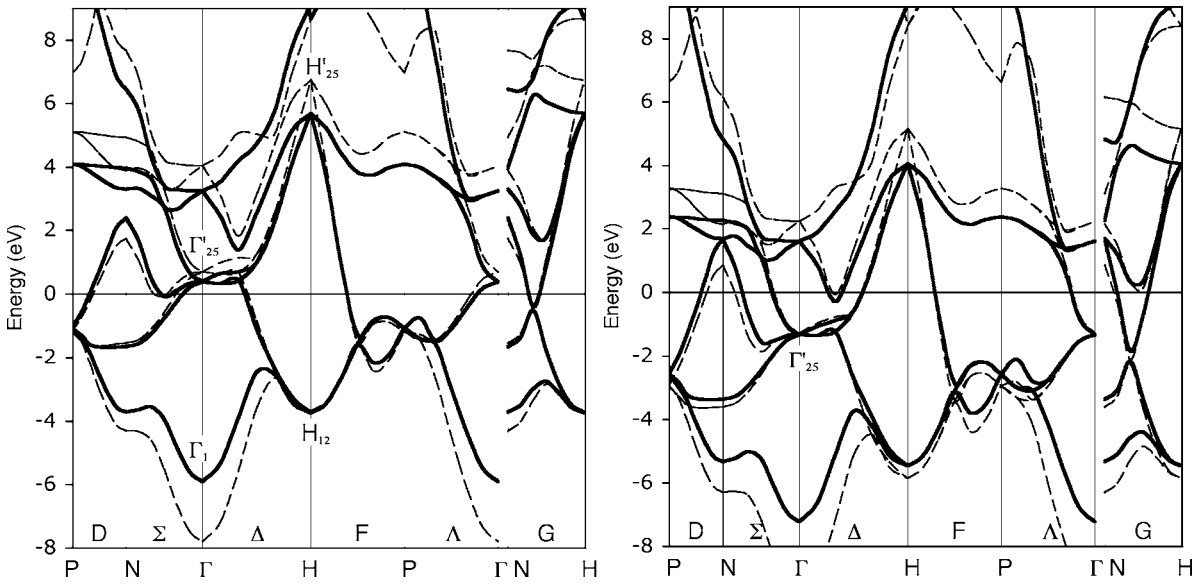

FIG. 2. Theoretical scalar-relativistic LDA ground-state band structures. The left panel shows niobium (solid bold line) and tantalum (dashed thin line), whereas the right panel shows molybdenum (solid bold line) and tungsten (dashed thin line).

filled and contribute to the Fermi surfaces, which are characterized by multiple sheets. Cross sections of the Fermi surfaces are shown in Fig. 3 for the group-VB metals in the left panel and for the group-VIB metals in the right panel. The colored areas indicate the regions of the Brillouin zone where the transitions between selected pairs of bands give the strongest contribution to the interband absorption. These couples are $2\rightarrow3$, $3\rightarrow4$, and $3\rightarrow5$ for the group-VB metals, and $4\rightarrow5$, $3\rightarrow4$, and $3\rightarrow5$ for the group-VIB metals. We will discuss them later in the paper. In the group-VB metals closed hole pockets around Γ arise due to band 2, and around the symmetry points N due to band 3. Furthermore, band 3 gives rise to an open surface with arms in the Δ directions which is often referred to as the "jungle-gym." The pocket around Γ and the jungle-gym show a symmetry-induced degeneracy along the Λ line caused by the doubly degenerate Λ_3 states. This degeneracy will be lifted by spin-orbit effects. The three metals show also another point of contact inside the ΓHP plane (as depicted in Fig. 3), which is accidental and lifted by spin-orbit effects as well. The hole pockets situated around the symmetry points N are also found in the group-VIB metals, as can be expected from the band structures. However, a quite different picture of the Fermi surface emerges for these metals due to the position of the Γ'_{25} states which now lie below the Fermi level. Hole pockets around H and an electron pocket around Γ appear due to bands 3 and 4, respectively. These two surfaces have a point of contact on the Δ line as the two bands show a symmetry-induced degeneracy, which again will be lifted by spin-orbit effects. In addition, another tiny pocket of electrons occurs along the Δ lines as contribution from band 5. As we will show later in this paper, transitions near the symmetry-induced degeneracies are responsible for the low-frequency interband absorption.

The analysis shows that the band dispersions of all six metals are very similar. We observe only minor differences between metals which are adjacent in the Periodic Table but at the same time we see larger changes within each group, in particular in the d-band width. The main difference between the group-VB and -VIB metals is in the filling of the d bands and, as result, in the topology of the Fermi surfaces. Since transitions between d bands are responsible for the main structure in the optical absorption spectra, we expect to find common features shifting in energy corresponding to the increase of the d-band dispersion within the group. The adjacent group will have features in common at very similar frequencies, but also different features will result from the difference in filling of the d bands and the topology of the Fermi surface.

B. Dielectric function

In Fig. 4 we report the calculated real and imaginary parts of the dielectric functions of V, Nb, and Ta in the left panels, and of Cr, Mo, and W in the right panels. The theoretical results are compared with our ellipsometry measurements and with other experiments present in literature.[1–3,10,11] For the 4d and 5d metals we found that relativistic effects are important. Therefore the results depicted for the 4d and 5d metals refer to scalar-relativistic calculations. A comparison with the nonrelativistic calculations of the dielectric functions is reported in Fig. 5. Upon inclusion of scalar-relativistic effects the dielectric functions of the group-VB metals Nb and Ta appear rigidly blueshifted and the intensity of some spectral features changes significantly with respect to the nonrelativistic spectra. In the group-VIB metals Mo and W, the absorption bandwidths become broader by including scalar-relativistic effects. In particular for Mo the double-peak structure at about 2 eV then becomes visible. Similarly the absorption peak at about 1 eV and the main features in the real part of the dielectric function of W are now correctly reproduced with respect to the experiments. Spin-orbit effects are not treated at the moment in our response calculations, but they can be important, in particular for the 5d

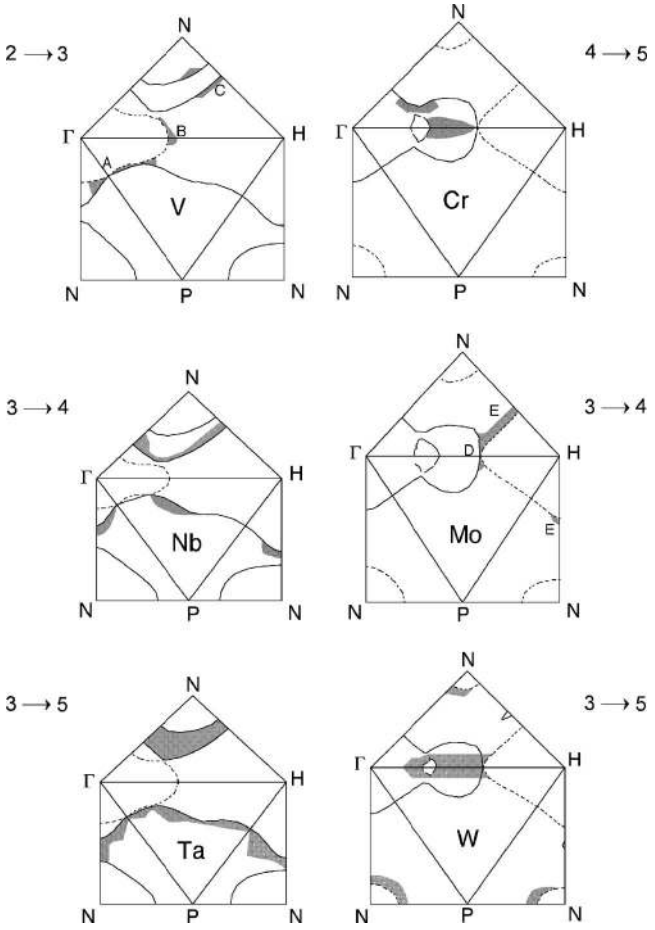

FIG. 3. Theoretical Fermi surface cross sections for V, Nb, Ta (left panel), and Cr, Mo, and W (right panel). The Brillouin zones have been plotted at the correct relative scale. The solid, the long dashed and the short dashed lines represent the contributions to the Fermi surface due to the bands 2, 3, and 4, respectively. The shaded regions indicate the regions in the Brillouin zone that contribute most to the absorption due to the transitions between the respective bands.

metals Ta and W. Indeed our results obtained by treating both the scalar- and spin-orbit effects in the ground-state calculations show that the spin-orbit coupling removes the degeneracy between, for example, bands 2 and 3 along Λ in the group-VB metals and between bands 3 and 4 along Δ in the group-VIB metals. This will effectively remove all points of contact of the Fermi-surface sheets, thus introducing a finite gap in the interband absorption spectra. In tungsten, for example, transitions near the Fermi surface between the two bands that would otherwise be degenerate but that are separated by about 0.60 eV upon inclusion of spin-orbit effects, are expected to be responsible for the sharp interband absorption onset found experimentally with a maximum at about 0.42 eV.[3] Our conclusions are in line with the findings of Antonov *et al.*,[37] who calculated the optical properties of several 5*d* metals within the random-phase approximation (RPA) and the fully relativistic linear muffin-tin orbital (LMTO) method. In the absorption spectrum of tungsten the low-frequency peak and onset are absent in their calculations which excluded spin-orbit effects, whereas they appear in the fully relativistic calculation. They associated this to the direct transitions between the two bands crossing the Fermi level in the neighborhood of the hygh-symmetry point *H* (bands 3 and 4 in our calculations). The degeneracy of these two bands is lifted by the spin-orbit coupling and a small energy gap appears, resulting in a finite absorption onset.

In our scalar-relativistic calculations the use of a linear interpolation for the evaluation of the *k*-space integrals in the response calculations might result in an incorrect description of the response in the very low-frequency region. For this reason we analyzed the topology of the Fermi surface at the singular points by using the $\mathbf{k}\cdot\mathbf{p}$ method. This analysis indicates a constant interband contribution to the absorption in the low-frequency region for each of the six metals. We determined the value for the low-frequency absorption below 0.5 eV by extrapolating the linear relation found at higher frequencies for the current-current response function vs ω^2. In our scalar-relativistic calculations the interband absorption extends all the way down to $\hbar\omega=0$ eV. For most metals, however, two regions can be distinguished in the absorption spectrum, being the low-frequency region in which intraband transitions are assumed to be dominant and that is well described by a Drude model, and the visible region where the interband absorption is most important. In the ALDA approach there is no intraband contribution to the imaginary part of the dielectric function at finite frequency. Responsible for the Drude-like absorption are relaxation processes which are not described within the ALDA, in which a frequency-independent exchange-correlation kernel is used.[9] Therefore we can directly relate the calculated and experimental absorption spectra only at frequencies higher than $\sim$1 eV where, for the metals studied here, the Drude-like absorption is found to be small.[2,10] In the low-frequency region the comparison is more problematic. To overcome these difficulties we add to our calculated interband absorption an intraband contribution which we found to be well described by a simple Drude model,

$$\epsilon_2(\omega) = \epsilon_2^{inter}(\omega) + \epsilon_2^{D}(\omega), \tag{8}$$

where $\epsilon_2^{inter}(\omega)$ is the calculated interband contribution to the imaginary part of the dielectric function and $\epsilon_2^{D}(\omega)$ is the Drude contribution given by

$$\epsilon_2^{D}(\omega) = \frac{\omega_p^2 \tau}{\omega(1+\omega^2\tau^2)}, \tag{9}$$

with ω_p the plasma frequency and τ the relaxation time. Normally these two parameters are determined by fitting the bare Drude model to the experimental data below the onset of the interband transitions, where one assumes that the absorption is predominantly Drude like. In the present case, however, the Drude model alone cannot describe the low-frequency absorption, since even for the lowest frequency in the experimental window the interband absorption is non-negligible. Our calculated constant low-frequency absorption will lead to an extra term with a logarithmic divergence at small frequencies in the real part of the dielectric function. Indeed for

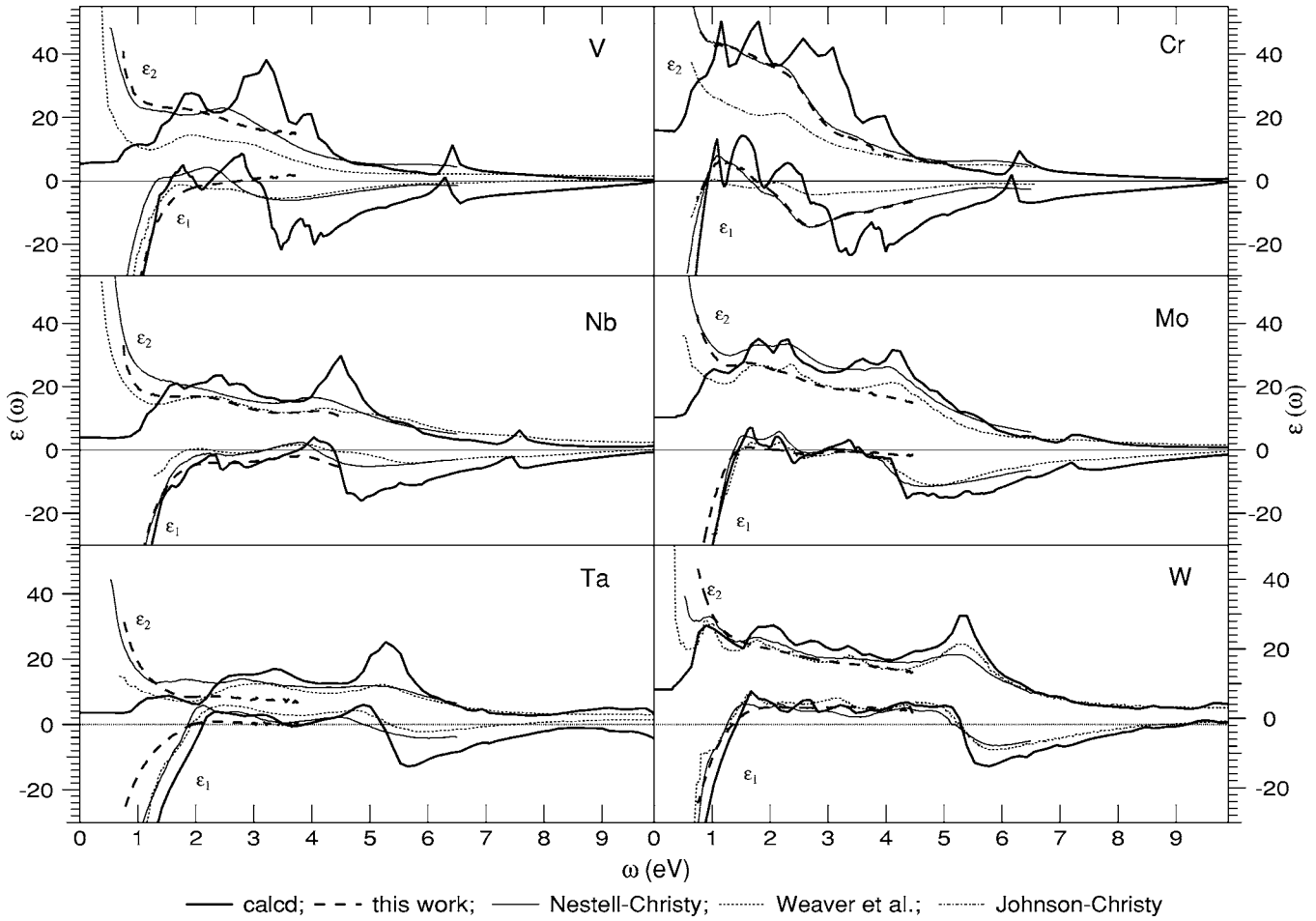

FIG. 4. The calculated (solid bold line) and measured (dashed thin line) dielectric functions for vanadium, niobium, tantalum, chromium, molybdenum, and tungsten. Our measurements have been performed as described in Sec. I, the other experimental results are taken from Refs. 1–3, 10, and 11. The theoretical curves reported for Nb, Ta, Mo, and W are results of scalar-relativistic calculations.

Nb, Ta, Mo, and W the plasma frequencies obtained by fitting the bare Drude model to experiments differ appreciably from the theoretical values.[38–40] This was associated with a renormalization of the optical mass by Fermi-liquid effects[38] rather than to interband processes. We found that Eq. (8) still holds and that Eq. (9) can describe the intraband part of the low-frequency absorption. Here the Drude parameters are obtained in the following way. We subtract the calculated interband absorption from the experimental curve (comprising both inter- and intraband contributions) and fit Eq. (9) to the remaining part. In this fit we use the calculated value for ω_p, which is directly related to the intraband contribution to the macroscopic optical conductivity,[7] $\omega_p^2 = -4\pi i\omega\sigma^{intra}(\omega)$, and we obtain the optimal relaxation time via a least-squares procedure. The Drude parameters thus obtained are listed in Table I. In order to test the quality of our calculations we want to compare the calculated interband absorption with the experiments. To do this we subtract from the experimental absorption the intraband contribution described by Eq. (9) in which we use the theoretical value for the plasma frequency and the fitted relaxation time. The result of this procedure is depicted in Fig. 6, where we have also reported the Drude-like tail. We are now ready to assign the spectral features to interband processes. The position of the main features in the experimental spectra were obtained by using the extrema in the second derivative of the interband spectrum and they are given in Tables II and III.

1. Assignment of the interband spectra

In order to facilitate the comparison of the spectral features we interpreted the absorption spectra in terms of direct transitions between couples of bands. In Fig. 7 we reported the main contributions to the absorption spectra. The first and second peaks common to the 3*d* and 4*d* metals can be attributed mainly to the transitions $3 \rightarrow 4$ and $3 \rightarrow 5$, respectively, whereas the shoulder at low frequency is mainly due to the transitions $2 \rightarrow 3$ for the group-VB metals and to the transitions $4 \rightarrow 5$ for the group-VIB metals. It becomes clear that in Ta the broad peak centered at about 3.1 eV can be related to the first absorption peak which appears also in the 3*d* and 4*d* metals, whereas the peak at about 1.4 eV can be related to the shoulder present in the other group-VB metals. We find again that the same couples of bands, which are mainly responsible for the first absorption peak observed for the group-VIB metals Cr and Mo, are also involved in the absorption spectrum of W below 4 eV. Here different peaks are visible, revealing that a broader range of energies is covered by transitions between the two bands in different parts of the

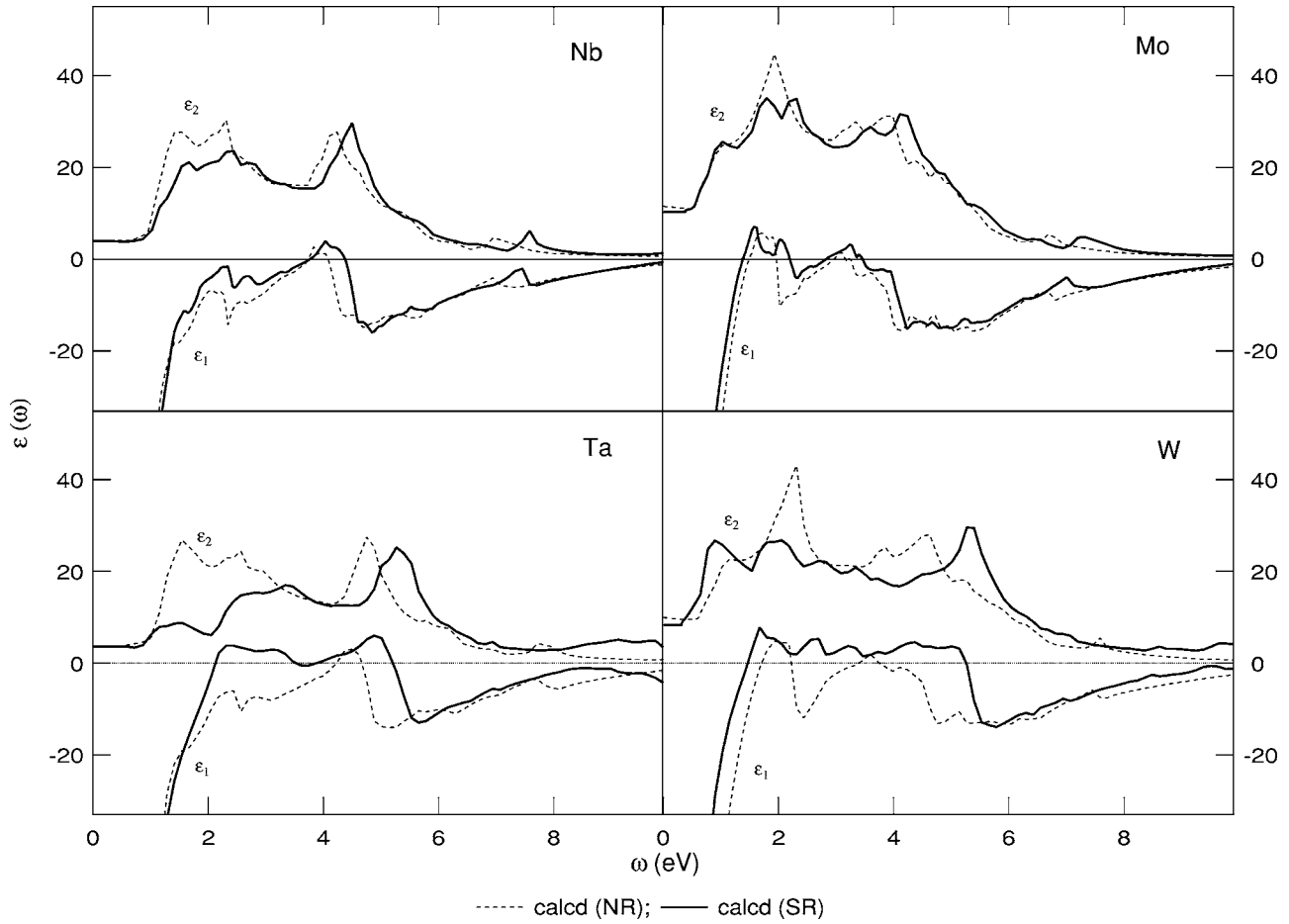

FIG. 5. Comparison between nonrelativistic and scalar-relativistic calculations of the dielectric functions of niobium, tantalum, molybdenum, and tungsten.

Brillouin zone. This is in keeping with the larger dispersion of the *d* bands in W as compared to Cr and Mo. All these metals show strong interband absorption also at very low frequencies, in line with absorbance measurements on Nb and Mo,[41] and calculations on Nb.[42] At frequencies below ~0.5 eV, the interband absorption becomes constant in our calculation, being larger in the group-VIB than in the group-VB metals. This very low-frequency interband absorption reveals a degeneracy of energy bands at the Fermi surface. We will analyze later the topology of the Fermi surface around the points of degeneracy which are involved in the low-frequency absorption. Unfortunately, not much experimental data is available at so low frequencies since optical experiments are difficult to perform as here the reflectivity is close to 1. However, structure in the low-frequency region $\omega < 1$ eV has been observed in Nb,[1,43] but it has been found to vary with sample preparation. By analyzing the transition dipole moments for transitions between pairs of bands we can visualize the regions of the Brillouin zone where the transitions give the strongest contribution to the interband absorption. In Fig. 3 the shaded areas indicate the regions where transitions give rise to the strongest absorption. We found that for metals within a group the same areas are involved, but also that the regions are somewhat more diffuse for the heaviest metals.

In the group-VB metals the absorption below 0.5 eV is due to the transitions $2 \rightarrow 3$ in the region which is indicated as A in Fig. 3, near the symmetry-induced degeneracy. Transitions between the same bands in the regions B and C are the main contribution to the shoulder at about 1 eV. The absorption in this low-frequency region is very similar for all three metals as the dispersion of bands 2 and 3 is only weakly modified within the group. The transitions $3 \rightarrow 4$ and $3 \rightarrow 5$ contribute mainly in the region just outside the junglegym part of the Fermi surface. Here, however, the corresponding absorption peaks will move within the group towards higher energies as result of the larger dispersion of the *d* bands, and hence of the increasing energy separation. These trends are clearly visible in the experiments and are well reproduced in our calculations, be it that the calculated peak positions are a few tenths to one-half of an eV too high.

In the group-VIB metals the transitions $3 \rightarrow 4$ contribute strongly to the low-frequency absorption in the region D around the point of degeneracy. The high-frequency part of the absorption that is due to these two bands originates from the region E. Passing via Mo to W the contribution from D in the ΓHP plane becomes stronger, resulting in a peak at about 1 eV instead of a shoulder, while the zone E becomes broader, resulting in a broad absorption over the whole spectral range 0–5 eV. The shoulder is also due to transitions

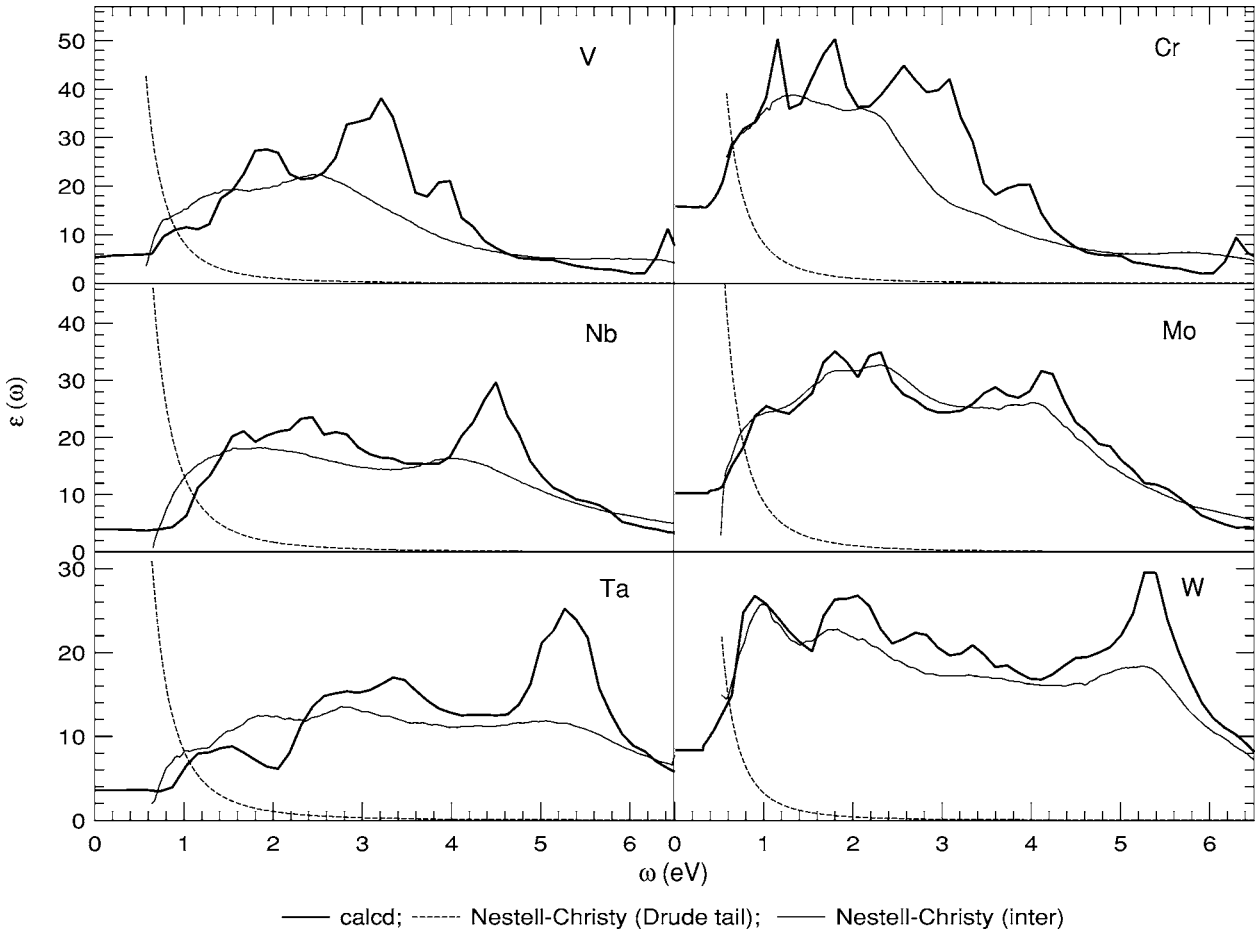

FIG. 6. Comparison between the measured and calculated interband contribution to the absorption spectra of vanadium, niobium, tantalum, chromium, molybdenum, and tungsten. The Drude absorption (intraband contribution to the experimental absorption, see text) is also reported. The experimental spectra used are taken from Ref. 10.

$4 \rightarrow 5$ mainly near the line Δ. From the same region, but also from the regions just outside the pockets around N transitions $3 \rightarrow 5$ give rise to the absorption in the high-frequency side of the spectrum. Again the increasing dispersion of the d bands within the group leads to a considerable shift of the spectral features. The trends in the experimental and theoretical spectra are again very similar as in the group-VB case. However, here the peak positions are generally well repro-

TABLE II. Position (in eV) of the main features in the experimental and theoretical spectra and their assignment in terms of transitions between pairs of bands for the group-VB metals.

	V		Nb		Ta	
Peak	Expt.[a]	ALDA	Expt.[a]	ALDA	Expt.[a]	ALDA
$2 \rightarrow 3$, A		<0.5[b]		<0.5[b]		<0.5[b]
$2 \rightarrow 3$, B, C	0.70	1.15	1.04	1.15,[c] 1.54	0.85, 1.50[d]	1.41
$3 \rightarrow 4$	1.25–1.48	1.92	2.20	2.31	1.81, 2.86	2.82, 3.34[e]
$3 \rightarrow 5$	2.50	3.11	4.04	4.49	5.33[f]	5.26
$1 \rightarrow 4$, $2 \rightarrow 5$	3.47	3.98		5.53		6.17
$1 \rightarrow 6$		6.43		7.60		9.40[g]

[a]Peak positions obtained using data from Ref. 10.
[b]Constant absorption: $\epsilon_2 = 5.33$, 3.94, and 3.60 for V, Nb, and Ta, respectively.
[c]Shoulder.
[d]Very weak shoulders.
[e]Here also the transitions $2 \rightarrow 4$ contribute.
[f]Broad peak.
[g]Broad; here also transitions $3 \rightarrow 6$ contribute.

TABLE III. Position (in eV) of the main features in the experimental and theoretical spectra and their assignment in terms of transitions between pairs of bands for the group-VIB metals.

	Cr		Mo		W	
Peak	Expt.[a]	ALDA	Expt.[a]	ALDA	Expt.[a]	ALDA
$3\rightarrow4$, D	-, 0.70	<0.5,[b] 0.77	-, 0.65	<0.5,[b] 1.08	-, 0.95	<0.5,[b] 0.90
$3\rightarrow4$, E	1.24	1.16, 1.80	1.77, 2.34	1.80, 2.31	1.78, 2.20,[c] 3.40[c]	1.90, 2.69, 3.34[d]
$3\rightarrow5$	2.32	2.57, 3.08	3.44, 4.08	3.60, 4.11	-, 4.98,[c] 5.36	3.72, 4.50, 5.40
$1\rightarrow4$	3.46[e]	3.85		5.39		6.81[f]
$1\rightarrow6$	5.83[e]	6.30		7.33		9.8[g]

[a]Peak positions obtained using data from Ref. 10.
[b]Constant absorption: $\epsilon_2=15.87$, 10.27, and 8.33 for Cr, Mo, and W, respectively.
[c]Very weak shoulder.
[d]Here also the transitions $3\rightarrow5$ contribute.
[e]Weak.
[f]Weak; here also transitions $2\rightarrow5$ and $3\rightarrow6$ contribute.
[g]Here also transitions $3\rightarrow6$ contribute.

duced except for the high-frequency range in Cr, where the peak positions are again overestimated by about one-half of an eV.

Our assignment of the spectra is in line with those reported in literature.[2,3,10,44,45] For the group-VB metals the first peak is mainly attributed to the transitions $\Sigma_1\rightarrow\Sigma_1$, which involves the third and fourth bands along the Σ line. Different transitions might contribute to the second peak: $\Delta_1\rightarrow\Delta_2'$ ($1\rightarrow5$ transitions), $D_4\rightarrow D_1'$ ($2\rightarrow4$ transitions), and $G_1\rightarrow G_4'$ ($1\rightarrow5$ transitions). However, this structure seems to arise from large regions of the Brillouin zone away from symmetry lines; in particular Pickett *et al.*[43] found that in Nb

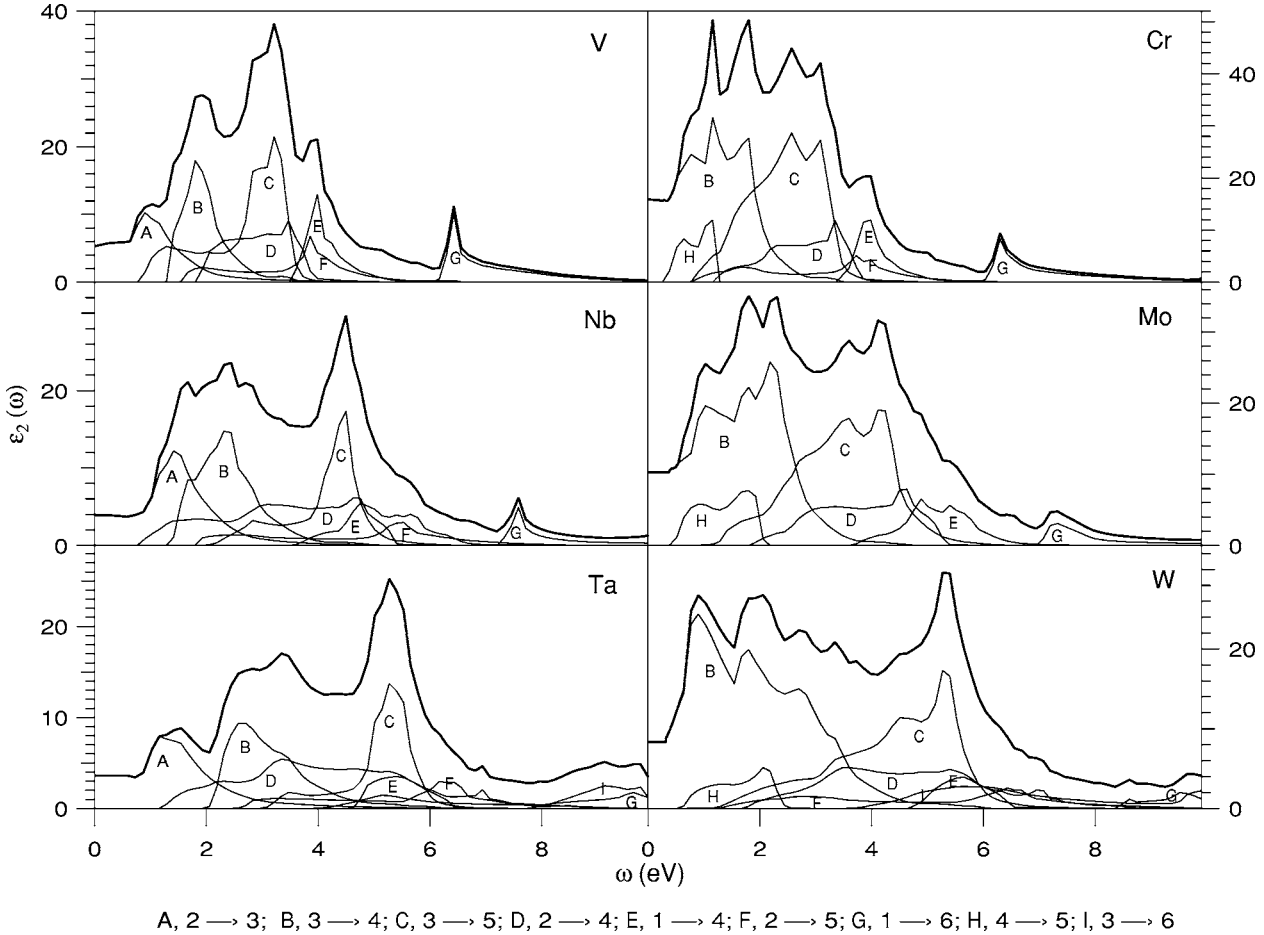

FIG. 7. Assignment of the absorption spectra. The figure shows the total intensity (bold line) and the decomposition in terms of the different contributions due to direct transitions between the indicated pairs of bands.

and Mo the peak is mainly due to $3\rightarrow 5$ transitions near $\mathbf{k}=(\frac{1}{2},\frac{1}{4},\frac{1}{4})$. In the group-VIB metals the transition $\Delta_5\rightarrow\Delta_2'$ (3, $4\rightarrow 5$ transitions) contributing to the absorption below 2 eV is common to the three metals. In Mo and W other transitions along the Δ line are found involving the third and fourth bands for Mo and W, and the fourth and fifth bands for W. Bands 3, 4, and 5 along Σ are found to be responsible for the structures at about 2.35 eV in Mo and at about 3.42 eV in W. The second peak in Cr is attributed to the transitions $\Delta_5\rightarrow\Delta_1$ ($3\rightarrow 6$ transitions) and $\Sigma_1\rightarrow\Sigma_4$ ($3\rightarrow 5$ transitions), whereas in Mo and W bands along F, G, Σ, and Λ, in particular the couples of bands 3 and 4, and 3 and 5, could all be contributing.

Our analysis shows that the spectra of the six metals are in general well reproduced by our calculations. Nevertheless, the locations of some absorption peaks deviate from the experimental ones, in particular in the 3*d* metals. The assignments of the absorption spectra in terms of *d*-*d* transitions and the analysis of the regions in the Brillouin zone where they mainly occur indicate that transitions from the Fermi level to virtual bands 4 and 5 yield absorption peaks that are blueshifted with respect to the experiments. The deviation is mainly observed in the 3*d* metals and decreases within a group. In the 4*d* and 5*d* group-VIB metals Mo and W these deviations are almost nonexisting. From the band structures it becomes clear that the energy separation with the Fermi level of these virtual bands strongly increases while their dispersions remain almost unchanged, resulting within a group in a shift of the absorption peaks towards higher frequencies. On the other hand, absorption peaks are better reproduced if they are due to transitions between bands close to the Fermi level, namely bands 2 and 3, which show very similar dispersions for the metals within the same group. These findings suggest that virtual *d* bands are too weakly bound by using the local density approximation (or standard gradient corrected approximations) to the ground-state exchange-correlation functional, in particular in the 3*d* metals.

2. $\mathbf{k}\cdot\mathbf{p}$ *analysis of the low-frequency interband transitions*

We mentioned above that the linear tetrahedron method is not very reliable to solve the *k* integrals in our response calculations for the absorption spectra in the very low-frequency region. The low-frequency absorption, indeed, involves bands degenerate at the Fermi surface, for which a more accurate description of the dispersion is required. In order to fully understand the low-frequency behavior of the absorption spectra and the differences between the group-VB and -VIB transition metals, we studied the interband contribution to the imaginary part of the dielectric function. If we neglect the local-field effects and the relativistic corrections in our method this contribution is given for isotropic systems by[7]

$$\mathrm{Im}\{\epsilon^{inter}(\omega)\}=\frac{1}{6\pi}\sum_{i,a}\int d\mathbf{k}\frac{|\langle\psi_{i\mathbf{k}}|\hat{\mathbf{j}}|\psi_{a\mathbf{k}}\rangle|^2}{(\epsilon_{i\mathbf{k}}-\epsilon_{a\mathbf{k}})^2}\times[\delta(\epsilon_{i\mathbf{k}}-\epsilon_{a\mathbf{k}}+\omega)-\delta(\epsilon_{i\mathbf{k}}-\epsilon_{a\mathbf{k}}-\omega)], \tag{10}$$

where i labels the occupied states, $\epsilon_{i\mathbf{k}}\leqslant\epsilon_F$, and a labels the unoccupied states, $\epsilon_{a\mathbf{k}}\geqslant\epsilon_F$, with ϵ_F the Fermi energy. We analyzed the dispersion of the touching bands 2 and 3 in group VB and of bands 3 and 4 in group VIB around their points of degeneracy at the Fermi level (as depicted in Fig. 3). At these points the integrand in Eq. (10) becomes singular. To evaluate the integrals in these points we made use of the $\mathbf{k}\cdot\mathbf{p}$ method of analytic continuation.[27] In this method the Bloch functions at $\mathbf{k}+\mathbf{q}$ can be expressed in terms of the eigenstates at the reference point $\mathbf{k}$ using

$$\psi_{\mathbf{k}+\mathbf{q}}(\mathbf{r})=\exp(i\mathbf{q}\cdot\mathbf{r})\sum_m\psi_{m\mathbf{k}}(\mathbf{r})c_{mn}(\mathbf{q}), \tag{11}$$

where the coefficients $c_{mn}(\mathbf{q})$ are solutions of the following eigenvalue equation:

$$\sum_m\left[\left(\frac{1}{2}q^2-\epsilon_{n\mathbf{k}+\mathbf{q}}+\epsilon_{m\mathbf{k}}\right)\delta_{lm}+\langle\psi_{l\mathbf{k}}|\mathbf{q}\cdot\mathbf{p}|\psi_{m\mathbf{k}}\rangle\right]c_{mn}(\mathbf{q})=0, \tag{12}$$

with $\mathbf{p}=-i\nabla$. The coefficients explicitly depend on the length and direction of $\mathbf{q}$. In our case the reference points are the points of degeneracy. The corresponding eigenvalues $\epsilon_{n\mathbf{k}+\mathbf{q}}$ give the energy dispersions, which can be expressed in a unidirectional Taylor series with $q\geqslant 0$ as

$$\epsilon_{n\mathbf{k}+\mathbf{q}}=\epsilon_{n\mathbf{k}}+qP_n(\hat{\mathbf{q}})+\frac{1}{2}q^2M_n^{-1}(\hat{\mathbf{q}})+\cdots, \tag{13}$$

where we introduced the group velocity $P_n(\hat{\mathbf{q}})$ and the effective mass $M_n(\hat{\mathbf{q}})$. By inserting $\mathbf{q}=\mathbf{0}$ in Eq. (12), it immediately follows that the coefficients $c_{mn}(\mathbf{0})$ can only be different from zero if $\epsilon_{m\mathbf{k}}=\epsilon_{n\mathbf{k}}$, hence we can limit the analysis to the degenerate subspace. By retaining only the terms linear in q it also follows that the coefficients diagonalize the subblock of the $\hat{\mathbf{q}}\cdot\mathbf{p}$ matrix built by the degenerate states, resulting in

$$P_n(\hat{\mathbf{q}})=\langle\psi_{n\mathbf{k}+\delta\mathbf{q}}|\hat{\mathbf{q}}\cdot\mathbf{p}|\psi_{n\mathbf{k}+\delta\mathbf{q}}\rangle. \tag{14}$$

For states that remain degenerate to first order in q these coefficients also diagonalize the corresponding subblock of the effective-mass matrix giving

$$M_n^{-1}(\hat{\mathbf{q}})=1+2\sum_{i,\epsilon_{n\mathbf{k}}\neq\epsilon_{i\mathbf{k}}}\frac{\langle\psi_{n\mathbf{k}+\delta\mathbf{q}}|\hat{\mathbf{q}}\cdot\mathbf{p}|\psi_{i\mathbf{k}}\rangle\langle\psi_{i\mathbf{k}}|\hat{\mathbf{q}}\cdot\mathbf{p}|\psi_{n\mathbf{k}+\delta\mathbf{q}}\rangle}{\epsilon_{n\mathbf{k}}-\epsilon_{i\mathbf{k}}}, \tag{15}$$

which contains the terms of order q^2. Here for notational convenience we have introduced the analytically continued eigenstates for the direction $\hat{\mathbf{q}}$,

$$\psi_{n\mathbf{k}+\delta\mathbf{q}}=\sum_m\psi_{m\mathbf{k}}c_{mn}^{(0)}(\hat{\mathbf{q}}), \tag{16}$$

where the coefficients $c_{mn}^{(0)}(\hat{\mathbf{q}})$ are given by

$$c_{mn}^{(0)}(\hat{\mathbf{q}})=\lim_{q\downarrow 0}c_{mn}(q\hat{\mathbf{q}}). \tag{17}$$

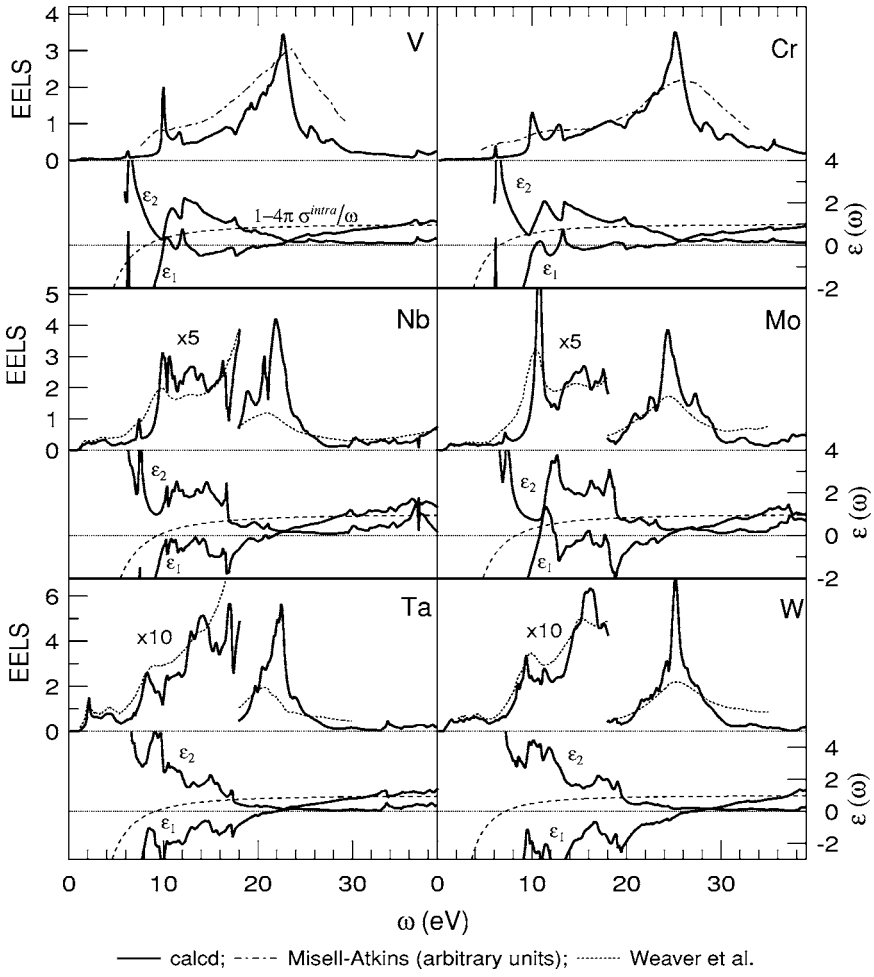

FIG. 8. Electron energy-loss spectra for vanadium, niobium, tantalum, chromium, molybdenum, and tungsten. The experimental results are taken from Refs. 1–3 and 46. The calculated real and imaginary parts of the dielectric function are also reported in the range 6–40 eV. The calculated results reported for Nb, Ta, Mo, and W refer to scalar-relativistic calculations.

Using the same expansion Eq. (11) one readily derives

$$\begin{aligned}\langle\psi_{i\mathbf{k}+\mathbf{q}}|\hat{\mathbf{j}}|\psi_{a\mathbf{k}+\mathbf{q}}\rangle &= \langle\psi_{i\mathbf{k}+\delta\mathbf{q}}|\hat{\mathbf{j}}|\psi_{a\mathbf{k}+\delta\mathbf{q}}\rangle + \mathbf{q}\,\delta_{ia} \\ &+ \sum_{n,\epsilon_{n\mathbf{k}}\neq\epsilon_{i\mathbf{k}}} \frac{\mathbf{q}\cdot\langle\psi_{i\mathbf{k}+\delta\mathbf{q}}|\mathbf{p}|\psi_{n\mathbf{k}}\rangle\langle\psi_{n\mathbf{k}}|\mathbf{p}|\psi_{a\mathbf{k}+\delta\mathbf{q}}\rangle}{\epsilon_{i\mathbf{k}}-\epsilon_{n\mathbf{k}}} \\ &+ \sum_{n,\epsilon_{n\mathbf{k}}\neq\epsilon_{a\mathbf{k}}} \frac{\langle\psi_{i\mathbf{k}+\delta\mathbf{q}}|\mathbf{p}|\psi_{n\mathbf{k}}\rangle\langle\psi_{n\mathbf{k}}|\mathbf{p}|\psi_{a\mathbf{k}+\delta\mathbf{q}}\rangle\cdot\mathbf{q}}{\epsilon_{a\mathbf{k}}-\epsilon_{n\mathbf{k}}} + \cdots . \end{aligned} \tag{18}$$

Details of this analysis for the six bcc metals can be found in the Appendix. We only state the results here. We find that in the group-VB metals bands 2 and 3 give rise to a linear conical intersection with the contact point as result of the symmetry-induced degeneracy positioned on the line Λ, which is also the axis of the cone. The degeneracy is lifted to first order in q for directions perpendicular to the axis, but it remains present for directions along the axis. From the $\mathbf{k}\cdot\mathbf{p}$ analysis it follows that the contribution to the absorption at low frequency due to the transitions $2\rightarrow3$ is constant. Similar results are found also for the point of accidental degeneracy. For the group-VIB metals, the bands 3 and 4 also give rise to a conical intersection with the axis of the cone along Δ (taken here as the $\hat{\mathbf{y}}$ direction). However, the degeneracy is lifted only to second order in q within the $\hat{\mathbf{x}}\hat{\mathbf{z}}$ plane, whereas it remains degenerate to all orders in q along Δ due to symmetry. The contribution to the absorption at low frequency due to the transitions $3\rightarrow4$ is found to be constant. We conclude that in our scalar-relativistic calculations the interband contribution to the absorption does not vanish at low frequencies but remains finite in these metals.

C. Electron energy-loss function

In Fig. 8 the calculated energy-loss function at $\mathbf{q}=\mathbf{0}$, $\mathrm{Im}\{-\epsilon(\omega)^{-1}\}$, is depicted in the range 0–40 eV for the six metals together with experiments reported in literature.[1–3,46] Three main regions can be identified in the electron energy-loss spectra (EELS): a low-frequency region up to 10 eV with small EELS intensities, a medium-frequency range starting with peak structures at about 10 eV and extending up to about 20 eV, and finally a high-frequency region that is dominated by a single intense peak at about 24 eV. The main peaks in the medium- and high-frequency regions have been identified as volume plasmons, be it of different nature:[1–3] the one at high frequency corresponding to the collective motion of all valence electrons and the medium-frequency ones involving only groups of electrons. For all metals a single peak in the medium-frequency region is usually identified as plasmonlike, except for tungsten where a second

TABLE IV. Position (in eV) of the main features in the experimental and theoretical electron-energy-loss spectra for the group-VB metals. Ω_p=free-electron-like plasmon peak; $\Omega_{1,2}$ =other main features.

	V		Nb		Ta	
Peak	Expt.[a]	ALDA	Expt.[a]	ALDA	Expt.[a]	ALDA
Ω_p	23.6	22.7	20.8	21.8	20.7	22.6
Ω_1	9.6	10.0	9.7	10.4	8.9	8.8
Ω_2			13.0	13.3	13.6	14.0

[a]Peak positions obtained using data from Refs. 1, 2, and 46.

peak can be seen at about 15.2 eV. In view of the occurrence of this second peak Weaver *et al.*[3] indicated that also in the other group-VIB metals and in the group-VB metals a second plasmon resonance should appear. Our ALDA calculations reproduce very well the experimental spectra in the low- and medium-frequency ranges: both the relative intensity and the position of the plasmon peaks are correctly described. The calculated plasmon peak in the high-frequency range, however, is too intense as compared to experiments for the 4*d* and 5*d* metals, but it appears at the correct position. Also in the 3*d* metals the position is correct, but here we cannot comment on the intensity as the experiments are given in arbitrary units. The main resonances are listed in Tables IV and V. The agreement between calculations and measurements is better for the electron energy-loss functions than for the dielectric functions. Although closely related, the two quantities depend in a different way on the long-range Coulomb interaction.[47] Whereas the dielectric function measures the macroscopic response to the macroscopic field, which includes the long-range screening of the external field, EELS measures the macroscopic response to an unscreened external field. By calculating the self-consistent response to the macroscopic field the long-range part of the Coulomb interaction is effectively removed from the self-consistent field.[12] In the EELS this dominant contribution to the self-consistent field remains present. As a result the dielectric function will be more sensitive to the quality of the approximations used for the much smaller exchange-correlation part of the self-consistent potentials. In many cases the ALDA approximation already gives a good description of the EELS, whereas more sophisticated approximations are required to describe correctly the dielectric function.

In all six metals the dominant plasmon resonance appears in the experiments at much higher frequency than the Drude free-electron plasma frequency. From our calculations it becomes clear that the shift in energy is completely due to the interplay between inter- and intraband effects. The free-electron resonance is renormalized due to the polarizable background that is introduced by the low-frequency interband processes. If only intraband processes were to be included the bulk plasmon resonance would occur at just below 10 eV. Upon inclusion of interband processes this resonance is shifted by approximately 10–15 eV to much higher energies. In the low-frequency region the intraband processes give rise to a very strong response, thus suppressing the EELS intensity. At about 10 eV, i.e., the Drude free-electron plasma frequency, the intraband response is minimal and interband processes start to dominate. Interband transitions give rise to a rich structure in the dielectric function, which in turn leads to additional plasmonlike features in the EELS. At frequencies where both ϵ_1 and ϵ_2 are small such plasmonlike resonances are clearly observed in the calculated and measured spectra. Even though these resonances are close to the Drude plasma frequency they are not free-electron-like resonances in nature, but they are caused by strongly mixed inter- and intraband processes. These features as well as the main plasmon resonances are very well reproduced in our calculations, in which local-field effects are fully included, and exchange-correlation effects are treated within the adiabatic local density approximation.

TABLE V. Position (in eV) of the main features in the experimental and theoretical electron-energy-loss spectra for the group-VB metals. Ω_p=free-electron-like plasmon peak; $\Omega_{1,2}$ =other main features.

	Cr		Nb		W	
Peak	Expt.[a]	ALDA	Expt.[a]	ALDA	Expt.[a]	ALDA
Ω_p	25.7	25.2	24.4	24.5	25.3	25.1
Ω_1	12.0	11.7	10.4	10.8	10.0	9.9
Ω_2			14.6	15.4	15.2	15.5

[a]Peak positions obtained using data from Refs. 2, 3, and 46.

VI. CONCLUSIONS

We have systematically analyzed the optical properties of the group-VB bcc transition metals V, Nb, and Ta, and the group-VIB bcc transition metals Cr (in the paramagnetic phase), Mo, and W by comparing theoretical and experimental results. The dielectric and electron energy-loss functions of these metals have been calculated by using our formulation of the linear response of metals within the time-dependent current-density-functional theory. Our calculations have been compared with our ellipsometry measurements of the dielectric functions and with other experiments reported in literature. The two sets of experimental data by Nestell, Johnson, and Christy and by Weaver and co-workers differ mostly on the low-frequency side. We attribute this discrepancy to the Drude-like extrapolation model used by Weaver *et al.* in their Kramers-Kronig procedure, which is needed to extract the optical constants from the reflectivity data. This is confirmed by the very good agreement up to about 3 eV between the reflectivities that we extracted from the optical constants obtained by Nestell and Christy with those reported by Weaver *et al.* Our experiments are in good agreement with Nestell and Christy's data.

We found that metals belonging to the same group show common spectral features which are shifted in energy with the increase of the *d*-band dispersion. On the other hand, features common to metals which are adjacent in the Periodic Table are found at similar energies, but also different features result from the different filling of the *d* bands. By carefully treating the topology of the Fermi surface, we calculated interband absorption already at frequencies below 0.5 eV, and hence deviations from the Drude behavior that is

often assumed in the experimental analysis of the linear response are expected for these metals. In general both the real and imaginary parts of the dielectric functions are well reproduced by our calculations. However, some calculated peaks in the absorption spectra are blueshifted with respect to the experiments, in particular in the 3*d* metals. We observed that peaks that are mainly due to transitions between bands close to the Fermi level are reasonably well described in our calculations. These bands show similar dispersions within a group. Absorptions involving transitions from the Fermi level to virtual bands are calculated at energies higher than the experimental ones, in particular in the 3*d* metals. The energy separation of these virtual bands with the Fermi level strongly changes within a group while the dispersion roughly remains the same. This finding indicates that the virtual bands are too weakly bound in the ground state described by using the LDA and equally by the standard GGAs. A better functional should shift down these virtuals almost rigidly over ~0.5 eV with respect to the LDA in order to correctly describe the response features. The use of exchange-correlation functionals beyond the adiabatic local density approximation should introduce the relaxation effects in the response calculations, that is lacking in the ALDA. Such nonadiabatic functionals are expected to give a better agreement between calculations and experiments by describing the electron-electron scattering part of the low-frequency Drude-like absorption and by broadening and smoothing the spectral features as effects of a finite relaxation time. The EELS spectra are very well reproduced by our method. The six metals show a dominant plasmon resonance at about 22–24 eV, well above the Drude free-electron plasma frequency. Our analysis shows that the shift in energy is completely due to the interplay of inter- and intraband effects. Additional plasmonlike features are calculated in the range 10–15 eV and are due to the rich structure in the dielectric functions resulting from interband transitions.

APPENDIX: FERMI-SURFACE TOPOLOGY

1. Group-VB metals: Symmetry-induced degeneracy along Λ

We first analyzed bands 2 and 3 of the group-VB metals around their point of degeneracy along Λ. The results given here are obtained from our numerical ground-state calculations. By taking the vector $\mathbf{q}$ along the Λ direction, $\hat{\mathbf{q}}_{\parallel} = 1/\sqrt{3}(1,1,1)^T$, the projection along $\hat{\mathbf{q}}_{\parallel}$ of the momentum matrix $\mathbf{p}$ entering in Eq. (12) becomes for this degenerate subspace

$$\hat{\mathbf{q}}_{\parallel} \cdot \mathbf{p} = a\sqrt{3}\begin{pmatrix} 1 & 0 \\ 0 & 1 \end{pmatrix}, \tag{A1}$$

with double degenerate eigenvalues $\lambda_1 = \lambda_2 = a\sqrt{3}$. This means that bands 2 and 3 remain degenerate along this direction at least to first order in q as can be expected from symmetry. We analyzed then the angular dependence of the two energy bands in the direction perpendicular to the $\hat{\mathbf{w}} = \hat{\mathbf{q}}_{\parallel}$ axis, by considering the vector $\mathbf{q}$ as

$$\hat{\mathbf{q}}_{\perp}(\phi) = \cos(\phi)\hat{\mathbf{u}} + \sin(\phi)\hat{\mathbf{v}}, \tag{A2}$$

where $\hat{\mathbf{u}} = 1/\sqrt{2}(1,-1,0)^T$ and $\hat{\mathbf{v}} = 1/\sqrt{6}(1,1,-2)^T$ are the other two unit vectors of the new system of coordinates $(\hat{\mathbf{u}},\hat{\mathbf{v}},\hat{\mathbf{w}})$ with the origin in the degeneracy of bands 2 and 3. In this case we obtain

$$\hat{\mathbf{q}}_{\perp}(\phi) \cdot \mathbf{p} = b\sqrt{\frac{3}{2}}\begin{pmatrix} 0 & -ie^{i\phi} \\ ie^{-i\phi} & 0 \end{pmatrix}, \tag{A3}$$

with eigenvalues $\lambda_{\pm} = \pm b\sqrt{3/2}$ independent from the angle ϕ, and eigenvectors $\hat{\mathbf{c}}_{\pm} = 1/\sqrt{2}(\mp ie^{i\phi}, 1)^T$. As we move away from the Λ symmetry line the degeneracy is lifted as described by Eq. (13): one band increases in energy and the other one decreases with the same amount independent from the angle ϕ. We can conclude that bands 2 and 3 give rise to a linear conical intersection with the contact point on the symmetry line Λ which is also the axis of the cone. The energy dispersion is then given by

$$\epsilon_{\pm}(q_{\parallel}, q_{\perp}) = \epsilon_F + a\sqrt{3}q_{\parallel} \pm b\sqrt{\frac{3}{2}}q_{\perp} + \mathcal{O}(q_{\perp}^2, q_{\parallel}^2), \tag{A4}$$

which is characteristic of a conical intersection. The new eigenvalues $\epsilon_{i\mathbf{k}+\mathbf{q}}$ and $\epsilon_{a\mathbf{k}+\mathbf{q}}$ of bands 2 and 3 then give rise to the form

$$\epsilon_{i\mathbf{k}+\mathbf{q}} - \epsilon_{a\mathbf{k}+\mathbf{q}} = -b\sqrt{6}q_{\perp} + \mathcal{O}(q_{\perp}^2, q_{\parallel}^2), \tag{A5}$$

where we made use of the cylindrical coordinates $(q_{\perp}, q_{\parallel}, \phi)$. We find for a generic direction that the off-diagonal elements of the momentum matrix $\mathbf{p}$ are a nonzero constant to zeroth order in q, thus we obtain

$$|\langle \psi_{i\mathbf{k}+\mathbf{q}} | \hat{\mathbf{j}} | \psi_{a\mathbf{k}+\mathbf{q}} \rangle| = \sqrt{\frac{3}{2}}b + \mathcal{O}(q_{\perp}). \tag{A6}$$

From our $\mathbf{k}\cdot\mathbf{p}$ analysis of the degeneracies in the group-VB metals we can evaluate the integranl in Eq. (10), which then becomes

$$\mathrm{Im}\{\epsilon^{inter}(\omega)\} \propto \frac{4}{3\pi}\int_0^{2\pi} d\phi \int_0^{q} q_{\perp} dq_{\perp} \int_{-|b/a\sqrt{2}|q_{\perp}}^{|b/a\sqrt{2}|q_{\perp}} dq_{\parallel} \times \delta(-b\sqrt{6}q_{\perp} + \omega)\frac{1}{4q_{\perp}^2} = \frac{2}{|a|3\sqrt{3}}, \tag{A7}$$

where we have considered that the contribution from the Λ line is eight-fold. A similar accidental conical intersection occurs in the ΓHP plane, and we arrive at similar conclusions as the case discussed above. Here the intensity is lower than the other degeneracy, but the contribution is 24-fold.

2. Group-VIB metals: Symmetry-induced degeneracy along Δ

The first two partially occupied bands 3 and 4 show a point of degeneracy along the Δ symmetry line taken here in the $\hat{\mathbf{y}}$ direction. By taking the vector $\mathbf{q}$ along the Δ direction, $\hat{\mathbf{q}}_{\parallel} = (0,1,0)^T$, the projection along $\hat{\mathbf{q}}_{\parallel}$ of the momentum matrix $\mathbf{p}$ in Eq. (12) for this degenerate subspace becomes

$$\hat{\mathbf{q}}_{\parallel} \cdot \mathbf{p} = p_{\parallel} \begin{pmatrix} 1 & 0 \\ 0 & 1 \end{pmatrix}, \tag{A8}$$

whereas in the $\hat{\mathbf{x}}\hat{\mathbf{z}}$ plane we have, with $\hat{\mathbf{q}}_{\perp}(\phi) = \cos(\phi)\hat{\mathbf{x}} + \sin(\phi)\hat{\mathbf{z}}$,

$$\hat{\mathbf{q}}_{\perp} \cdot \mathbf{p} = \begin{pmatrix} 0 & 0 \\ 0 & 0 \end{pmatrix}. \tag{A9}$$

It is immediately clear that along the Δ symmetry line the degeneracy is not lifted and the two energies change linearly with $q_{\parallel}$. In the $\hat{\mathbf{x}}\hat{\mathbf{z}}$ plane the energies do not change to first order in $q_{\perp}$, but the degeneracy may still be lifted to second order. Therefore we analyzed the effective-mass matrix, which has the following form in the symmetry-induced degeneracy along the symmetry line Δ:

$$M_{\parallel}^{-1} = m_{\parallel}^{-1} \begin{pmatrix} 1 & 0 \\ 0 & 1 \end{pmatrix}, \tag{A10}$$

$$M_{\perp}^{-1}(\phi) = \begin{pmatrix} \bar{m}_{\perp}^{-1} + \Delta_1 \cos(2\phi) & \tilde{\Delta}_2 \sin(2\phi) \\ \tilde{\Delta}_2^{*} \sin(2\phi) & \bar{m}_{\perp}^{-1} - \Delta_1 \cos(2\phi) \end{pmatrix}, \tag{A11}$$

with $\bar{m}_{\perp}$, $m_{\parallel}$, and Δ_1 real numbers, and $\tilde{\Delta}_2$ a complex number. It is immediate to verify that in the $\hat{\mathbf{y}}$ direction the degeneracy is not lifted even to second order, whereas it is lifted in the $\hat{\mathbf{x}}\hat{\mathbf{z}}$ plane as becomes clear from the form of the matrices in Eqs. (A10) and (A11). The energy dispersion is then given by

$$\epsilon_{\pm}(q_{\parallel}, q_{\perp}, \phi) = \epsilon_F + p_{\parallel} q_{\parallel} + \frac{1}{2} m_{\parallel}^{-1} q_{\parallel}^2 + \frac{1}{2} m_{\perp,\pm}^{-1}(\phi) q_{\perp}^2 + \mathcal{O}(q_{\perp}^3, q_{\parallel}^3), \tag{A12}$$

where

$$m_{\perp,\pm}^{-1}(\phi) = \bar{m}_{\perp}^{-1} \pm \sqrt{\Delta_1^2 \cos^2(2\phi) + |\Delta_2|^2 \sin^2(2\phi)}. \tag{A13}$$

Since $|\Delta_2| \approx \Delta_1 = \Delta$, we can consider $\Delta_2 = \Delta e^{i\zeta}$ without losing the validity of this analysis. In this case the eigenvectors have the form $\hat{\mathbf{c}}_{\pm} = 1/\sqrt{2 \mp 2\cos(2\phi)}[\pm 1 - \cos(2\phi), -\sin(2\phi)e^{-i\zeta}]^T$. The new eigenvalues $\epsilon_{i\mathbf{k}+\mathbf{q}}$ and $\epsilon_{a\mathbf{k}+\mathbf{q}}$ of bands 3 and 4 then lead to

$$\epsilon_{i\mathbf{k}+\mathbf{q}} - \epsilon_{a\mathbf{k}+\mathbf{q}} = -\Delta \cdot q_{\perp}^2 + \mathcal{O}(q_{\perp}^3), \tag{A14}$$

where we again used the cylindrical coordinates. We find for a generic direction that the off-diagonal elements of the momentum matrix $\mathbf{p}$ are linear in q, thus we obtain

$$|\langle \psi_{i\mathbf{k}+\mathbf{q}} | \hat{\mathbf{j}} | \psi_{a\mathbf{k}+\mathbf{q}} \rangle| = \Delta \cdot q_{\perp} + \mathcal{O}(q_{\perp}^2). \tag{A15}$$

We are now ready to evaluate Eq. (10) giving

$$\mathrm{Im}\{\epsilon^{inter}(\omega)\} \propto \frac{1}{\pi} \int_0^{2\pi} d\phi \int_0^{q} q_{\perp} dq_{\perp} \int_{\alpha_- q_{\perp}^2}^{\alpha_+ q_{\perp}^2} dq_{\parallel} \times \delta(-\Delta \cdot q_{\perp}^2 + \omega) \frac{1}{q_{\perp}^2} = \frac{1}{p_{\parallel}} \tag{A16}$$

with $\alpha_{\pm} = -1/2(\bar{m}_{\perp} \pm \Delta)/p_{\parallel}$. Here we have considered that the contribution from the Δ symmetry line is six-fold.

*Electronic address: P.L.de.Boeij@rug.nl

[1] J. H. Weaver, D. W. Lynch, and C. G. Olson, Phys. Rev. B **7**, 4311 (1973).
[2] J. H. Weaver, D. W. Lynch, and C. G. Olson, Phys. Rev. B **10**, 501 (1974).
[3] J. H. Weaver, C. G. Olson, and D. W. Lynch, Phys. Rev. B **12**, 1293 (1975).
[4] J. H. Weaver, C. G. Olson, M. Piacentini, and D. W. Lynch, Solid State Commun. **16**, 163 (1975).
[5] D. W. Lynch, C. G. Olson, and J. H. Weaver, Phys. Rev. B **11**, 3617 (1975).
[6] J. H. Weaver, Phys. Rev. B **11**, 1416 (1975).
[7] P. Romaniello and P. L. de Boeij, Phys. Rev. B **71**, 155108 (2005).
[8] P. Romaniello and P. L. de Boeij, J. Chem. Phys. **122**, 164303 (2005).
[9] R. van Leeuwen, Phys. Rev. B **69**, 115110 (2004).
[10] J. E. Nestell, Jr. and R. W. Christy, Phys. Rev. B **21**, 3173 (1980).
[11] P. B. Johnson and R. W. Christy, Phys. Rev. B **9**, 5056 (1974).
[12] F. Kootstra, P. L. de Boeij, and J. G. Snijders, J. Chem. Phys. **112**, 6517 (2000).
[13] F. Kootstra, P. L. de Boeij, and J. G. Snijders, Phys. Rev. B **62**, 7071 (2000).
[14] P. Nozières and D. Pines, *The Theory of Quantum Liquids* (Perseus Books, Cambridge, MA, 1999).
[15] F. Kootstra, P. L. de Boeij, H. Aissa, and J. G. Snijders, J. Chem. Phys. **114**, 1860 (2001).
[16] P. L. de Boeij, F. Kootstra, and J. G. Snijders, Int. J. Quantum Chem. **85**, 449 (2001).
[17] E. van Lenthe, E. J. Baerends, and J. G. Snijders, J. Chem. Phys. **101**, 9783 (1994).
[18] E. van Lenthe, R. van Leeuwen, E. J. Baerends, and J. G. Snijders, Int. J. Quantum Chem. **57**, 281 (1996).
[19] P. H. T. Philipsen, E. van Lenthe, J. G. Snijders, and E. J. Baerends, Phys. Rev. B **56**, 13556 (1997).
[20] G. te Velde and E. J. Baerends, J. Comput. Phys. **99**, 84 (1992).
[21] C. Fonseca Guerra, O. Visser, J. G. Snijders, G. te Velde, and E. J. Baerends, in *Methods and Techniques in Computational Chemistry*, edited by E. Clementi and G. Corongiu (STEF, Cagliari, 1995), p. 305.
[22] G. te Velde, Ph.D. thesis, Free University, Amsterdam, 1990.
[23] F. Herman and S. Skillman, *Atomic Structure Calculations* (Prentice-Hall, Englewood Cliffs, NJ, 1963).
[24] E. van Lenthe and E. J. Baerends, J. Comput. Chem. **24**, 1142 (2003).
[25] G. Lehmann and M. Taut, Phys. Status Solidi B **54**, 469 (1972).
[26] G. Wiesenekker and E. J. Baerends, J. Phys.: Condens. Matter **3**, 6721 (1991); G. Wiesenekker, G. te Velde, and E. J. Baerends, J.

Phys. C **21**, 4263 (1988).
[27] M. Lax, *Symmetry Principles in Solid State and Molecular Physics* (Dover Publications, Inc., Mineola, NY, 2001).
[28] P. Bagno, O. Jepsen, and O. Gunnarsson, Phys. Rev. B **40**, R1997 (1989).
[29] T. C. Leung, C. T. Chan, and B. N. Harmon, Phys. Rev. B **44**, 2923 (1991).
[30] A. Khein, D. J. Singh, and C. J. Umrigar, Phys. Rev. B **51**, 4105 (1995).
[31] D. J. Singh and J. Ashkenazi, Phys. Rev. B **46**, 11570 (1992).
[32] N. A. W. Holzwarth and Y. Zeng, Phys. Rev. B **49**, 2351 (1994).
[33] J. P. Perdew, in *Electronic Structure of Solids 1991*, edited by P. Ziesche and H. Eschrig (Akademie Verlag, Berlin, 1991), p. 11.
[34] A. D. Becke, Phys. Rev. A **38**, 3098 (1988).
[35] J. P. Perdew, Phys. Rev. B **33**, R8822 (1986).
[36] S. H. Vosko, L. Wilk, and M. Nusair, Can. J. Phys. **58**, 1200 (1980).
[37] V. N. Antonov, A. I. Bagljuk, A. Ya. Perlov, V. V. Nemoshkalenko, Vl. N. Antonov, O. K. Andersen, and O. Jepsen, Low Temp. Phys. **19**, 494 (1993).
[38] W. E. Pickett and P. B. Allen, Phys. Rev. B **13**, 1473 (1976).
[39] B. Chakraborty, W. E. Pickett, and P. B. Allen, Phys. Rev. B **14**, 3227 (1976).
[40] L. F. Mattheiss, L. R. Testardi, and W. W. Yao, Phys. Rev. B **17**, 4640 (1978).
[41] E. S. Black, D. W. Lynch, and C. G. Olson, Phys. Rev. B **16**, 2337 (1977).
[42] A. R. Jani, N. E. Brener, and J. Callaway, Phys. Rev. B **38**, 9425 (1988).
[43] W. E. Pickett and P. B. Allen, Phys. Rev. B **11**, 3599 (1975).
[44] J. H. Weaver, D. W. Lynch, C. H. Culp, and R. Rosei, Phys. Rev. B **14**, 459 (1976).
[45] E. Colavita, A. Franciosi, C. Mariani, and R. Rosei, Phys. Rev. B **27**, 4684 (1983).
[46] D. L. Misell and A. J. Atkins, Philos. Mag. **27**, 95 (1973).
[47] G. Onida, L. Reining, and A. Rubio, Rev. Mod. Phys. **74**, 601 (2002).